applied sciences

MDPI

Article

Effect of Iron Loading on the Catalytic Activity of Fe/N-Doped Reduced Graphene Oxide Catalysts via Irradiation

Kazi Rumanna Rahman [1], Kuan Ying Kok [2], Wai Yin Wong [1], Hsiharng Yang [3] and Kean Long Lim [1,*]

[1] Fuel Cell Institute, University Kebangsaan Malaysia, Bangi 43600, Selangor, Malaysia; P98484@siswa.ukm.edu.my (K.R.R.); waiyin.wong@ukm.edu.my (W.Y.W.)
[2] Malaysian Nuclear Agency, Kajang 43600, Selangor, Malaysia; kyk1000@nuclearmalaysia.gov.my
[3] Graduate Institute of Precision Engineering and Innovation and Development Center of Sustainable Agriculture (IDCSA), National Chung Hsing University, 145 Xingda Road, South District, Taichung City 402, Taiwan; hsiharng@dragon.nchu.edu.tw
* Correspondence: kllim@ukm.edu.my; Tel.: +60-3-8911-8494; Fax: +60-3-8911-8530

Featured Application: Fuel Cells.

Abstract: The aim of this study is to produce noble-metal-free oxygen reduction reaction (ORR) catalyst via irradiation. Gamma ray irradiation reduction has been utilized to produce N-doped reduced graphene oxide (rGO)-supported iron (Fe)-based catalysts, whose weight percent (wt.%) of Fe loading varies from 10% to 20%. In this study, the physicochemical properties of Fe/N-rGO with various loadings of Fe (10 wt.%, 15 wt.% and 20 wt.%) were explored through X-ray diffraction (XRD), field emission scanning electron microscopy-energy dispersive spectroscopy (FESEM-EDS), Raman spectroscopy and Fourier transform infrared spectroscopy (FTIR). XRD showed that a broad-peak nanocrystallite Fe_2O_3 phase formed. Raman spectroscopy revealed that Fe insertion increased the disordered GO structure. Fourier transform infrared (FTIR) demonstrated that N was functionalized into rGO. FESEM-EDX presented that Fe nanoparticles existed on the wrinkled rGO surface but their amount was low. Linear sweep voltammetry (LSV) was performed with a rotating disk electrode in 0.1 M KOH at a scanning rate of 20 mVs^{-1} and revolution rates of 400, 900 and 1600 rpm and the corresponding electron transfer numbers were investigated with a Koutecky–Levich model. This model indicated that the number of electron transfers of 20% Fe/N-rGO was above 2 and its performance toward ORR was higher than those of 10% Fe/N-rGO and 15% Fe/N-rGO.

Keywords: alkaline electrolyte; gamma irradiation; Koutecky–Levich relationship; oxygen reduction reaction

check for updates

Citation: Rahman, K.R.; Kok, K.Y.; Wong, W.Y.; Yang, H.; Lim, K.L. Effect of Iron Loading on the Catalytic Activity of Fe/N-Doped Reduced Graphene Oxide Catalysts via Irradiation. *Appl. Sci.* **2021**, *11*, 205. https://doi.org/10.3390/app11010205

Received: 16 November 2020
Accepted: 23 December 2020
Published: 28 December 2020

1. Introduction

Oxygen reduction reaction (ORR) at the cathode side of a fuel cell is slow. Its kinetics can be improved with high amounts of Pt-based catalysts but these catalysts increase a fuel cell's cost. For this reason, new and reliable nonprecious metal ORR catalysts with a performance comparable with that of Pt-based catalysts should be explored. For instance, nitrogen-doped carbon catalysts, which contain iron (Fe), cobalt (Co) and manganese (Mn), are considered the most encouraging Pt/C substitute because of the amplifying and synergistic effects between nitrogen, carbon support and transition metals [1–3]. Fe can bond with multiple nitrogen (N) atoms, which change the configuration and characteristics of Fe species, thereby improving the overall catalyst behavior [4]. The efficiency of Fe-based catalysts is strongly affected by the synthesis procedures and the nature of existing heteroatoms. The most prominent synthesis of Fe-based catalysts is pyrolysis, which improves the durability of carbon-based nonprecious catalysts [5,6]. A carbon structure assumes a critical function in deciding the catalytic activity. Hence, appropriate carbon, metal and nitrogen antecedents should be chosen to build an exceptionally alluring catalyst for ORR [7,8]. Graphene as a catalyst support helps increase catalytic activity and durability because of its high explicit surface area (2630 $m^2\ g^{-1}$) and high electrical conductivity [9–11]. Several graphene-type materials, such as graphene oxide (GO), reduced graphene oxide (rGO), carbon nanotube and carbon nanofiber, are used as catalyst supports. Among these catalyst supports, rGO has been the most widely explored; its thermal stability is better than that of GO [12,13]. rGO is derived from GO, which can be produced via chemical and thermal exfoliation, chemical vapor deposition or arc discharge [10,14]. However, these methods are not suitable for producing GO in large quantities. As such, modified Hummer's method is widely applied to produce GO and hydrazine hydrate is used as a reducing agent to subsequently reduce GO to rGO [15,16].

Gamma irradiation has been used to produce different metal, metallic compound and metal oxide nanoparticles [17]. It is an attractive, easy and environment-friendly method of producing graphene-based nanomaterials [18,19]. It also helps reduce metal ions and modifies carbon properties and chemical reactions on surfaces [20,21].

In this study, rGO was synthesized using modified Hummer's method and reduced with hydrazine hydrate. rGO, urea and iron catalyst at different loadings were irradiated with gamma rays to produce N-doped rGO-based Fe catalysts.

2. Materials and Methods

GO was produced via Hummer's method [18]. In this technique, 3.0 g of graphite powder was combined with 1.5 g of sodium nitrate and 100 mL of concentrated H_2SO_4 in a beaker in an ice bath. Afterward, 12.0 g of $KMnO_4$ was gradually added to the mixture and temperature was maintained under 5 °C. The mixture was stirred for 24 h. After 24 h, 150 mL of deionized (DI) water was poured gradually into the slurry and mixed for another 24 h. Then, 15 mL of 30 wt.% H_2O_2 was added to the slurry. Finally, the slurry was washed with 5% HCl and DI water multiple times to eliminate the overabundance of metal particles. The obtained brown dispersion was kept in an oven at 90 °C [15].

At the subsequent stage, GO was reduced with hydrazine hydrate. In this cycle, GO powder was dispersed in DI water (1 mg/mL) and ultrasonicated for 1 h at <50 °C to obtain a homogeneous suspension. Next, 2 mL of hydrazine hydrate was placed in 50 mL of the GO solution and pH was adjusted to 10. This solution was stored in an oven at 90 °C for 24 h. Afterward, the dried rGO powder was washed with DI water and methanol to achieve pH of ~7. The rGO suspension was kept in a hot air oven at 60 °C [22].

The liquid solutions were gamma irradiated under an inert atmosphere at room temperature under the conditions proposed by Park et al. [17]. A solid mixture of rGO and urea was prepared at a mass ratio of 3:1 (rGO:urea) [23]. Gray powder was added to a mixture of DI water and ethanol. Finally, 10%, 15% and 20% of iron (III) nitrate with a mass ratio of 3:1 (rGO:urea) were taken to prepare the solutions for catalyst synthesis. The range and ratios were adopted from Sudarsono et al. [7], Xi et al. [24] and Osmeiri et al. [25]. Afterward, the solutions were ultrasonicated for 30 min. N_2 was purged into the mixture for 15 min and sealed for irradiation. A ^{60}Co gamma irradiation source with a total dose of 100 kGy (a dose rate of 2 kGy/h) was used. After irradiation, the mixture was filtered with isopropanol and DI water and dried at room temperature.

A catalyst ink was prepared by mixing 10 μL of 5 wt.% Nafion, 100 μL of DIW, 890 μL of ethanol and 2 mg of catalyst. Then, the ink was dispersed in an ultrasonic sonicator for 30 min to acquire a homogeneous suspension. Next, 10 μL of the suspension was drop cast onto a glassy carbon terminal (GCE) and dried at room temperature [21].

Raman spectroscopy (Renishaw inVia Reflex) with an excitation laser of 532 nm wavelength was employed to evaluate the quality of the rGO produced from graphite powder. X-ray diffraction (XRD; Panalytical, X'pert Pro MPD) operated with Cu radiation in the range of 20° to 70° was applied to examine the phases of the compositions. A field emission scanning electron microscope (FESEM; Carl Zeiss, GeminiSEM 500) was utilized to explore the surface morphology of rGO and the catalysts. Fourier transform infrared (FTIR) (Bruker Tensor II) was carried out in the range of 700 cm^{-1} to 4000 cm^{-1}.

For rotating disk electrode (RDE) measurements, the required electrode was prepared in accordance with previously described methods [26]. Under oxygen (O_2) saturated conditions, a linear sweep voltammetry (LSV) test was performed with a scan rate of 20 mVs^{-1} in a rotation speed range of 400–1600 rpm [23–25] and in the potential range of 0.1 mV to −0.8 mV for all three catalysts. Current densities were calculated from LSV and normalized through the geometric surface. The number of electron transfers (n) was calculated with the Kouteky–Levich (K–L) equation [26–28]:

$$\frac{1}{J} = \frac{1}{J_K} + \frac{1}{B\omega^{1/2}}, \tag{1}$$

where

$$B = 0.62nFCo_2Do_2{}^{2/3}\ \upsilon^{-1/6,} \tag{2}$$

where J, J_K and ω are the measured current density, kinetic limiting current density and rotating speed of the electrode, respectively; F is the Faraday constant (96,485 C mol^{-1}); Co_2 is the bulk concentration of O_2 electrolyte (1.2×10^{-6} mol cm^{-3}); D_{O2} is the diffusion coefficient of O_2 in the electrolyte (1.9×10^{-5} cm^2 s^{-1}); and υ is the kinetic viscosity (0.01 cm^2 s^{-1}).

3. Results and Discussion

3.1. X-ray Diffraction Analysis

The X-ray diffraction (XRD) patterns of the nonirradiated rGO and the irradiated Fe/N-rGO are presented in Figure 1a,b, respectively.

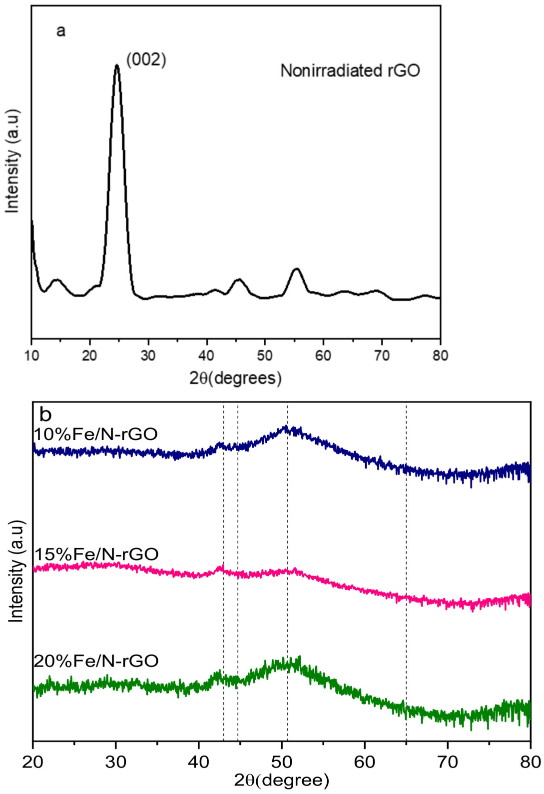

Figure 1. (**a**) X-ray diffraction (XRD) patterns of reduced graphene oxide (rGO) (before irradiation) and (**b**) 10% Fe/N-rGO, 15% Fe/N-rGO and 20% Fe/N-rGO.

In Figure 1a, one main peak was observed at 2θ = 24.67°, corresponding to the (002) plane of the rGO phase with the calculated d-spacing of 0.36 nm. Both peak positions and inter-planar distance confirmed the formation of rGO. rGO exhibited its characteristic peak in the range of 20° to 30°. Generally, the XRD pattern of rGO displays a broad peak with a low intensity. The peak intensity corresponding to the (002) plane indicates that some oxygenated species are present in the sample. Graphite exhibits a peak at 2θ of ~26.5°, corresponding to the (002) plane, whereas a GO peak appears at 2θ of 11.49°, corresponding to the (100) plane [12,15,29–31]. In Figure 1b, no sharp and narrow peak was observed. This amorphous XRD pattern confirmed the presence of Fe nanoparticles in the samples. The characteristic peaks of rGO in Figure 1a are not detected in Figure 1b possibly because of the existence of iron compounds that overwhelm the weak carbon peaks. Nevertheless, the broad peaks were likely attributed to the α-Fe_2O_3 phase and the particle size was at a nanoscale.

3.2. Raman Spectroscopy Analysis

Raman spectroscopy was performed to characterize the samples and elucidate the carbon structure. In Figure 2, all the samples possessed two characteristic peaks at ~1348 (D band) and ~1598 (G band) cm^{-1}. The 2D band intensity of rGO and GO normally appears at around 2700 cm^{-1} but it was completely absent in all the three samples in this study. The absence of the 2D band intensity confirmed that the structure had high amount of defects. The 2D peak intensity depends on electron doping and structural disorders [32,33]. In our study, the D band resulted from structural imperfection caused by the presence of the disordered carbon and the G band was attributed to the E_{2g} vibration of carbon atoms. The intensity ratio of the D and G bands (I_D/I_G) was used to estimate the defects of the samples. Our results revealed that 10% Fe/N-rGO, 15% Fe/N-rGO and 20% Fe/N-rGO had I_D/I_G of 0.69, 0.65 and 0.71, respectively, suggesting that 20% Fe/N-rGO had the highest amount of defects [18]. I_D/I_G is closely related to the sp^3/sp^2 carbon hybridization ratio. The sp^2-hybridized carbon is assigned to the carbon graphitic structure, whereas the sp^3 carbon hybrid is assigned to the bond between carbon and atoms such as nitrogen, oxygen and iron anchored on the carbon surface. Furthermore, 15% Fe/N-rGO showed the lowest ID/IG, suggesting that the low amount of Fe or few point defects [34–37] were introduced to the rGO structure. The result was consistent with the XRD results, which demonstrated that the lowest peak intensity among the three samples and the semi-quantitative EDS results reported in Table 1 reaffirmed the lowest Fe content of 15% Fe/N-rGO.

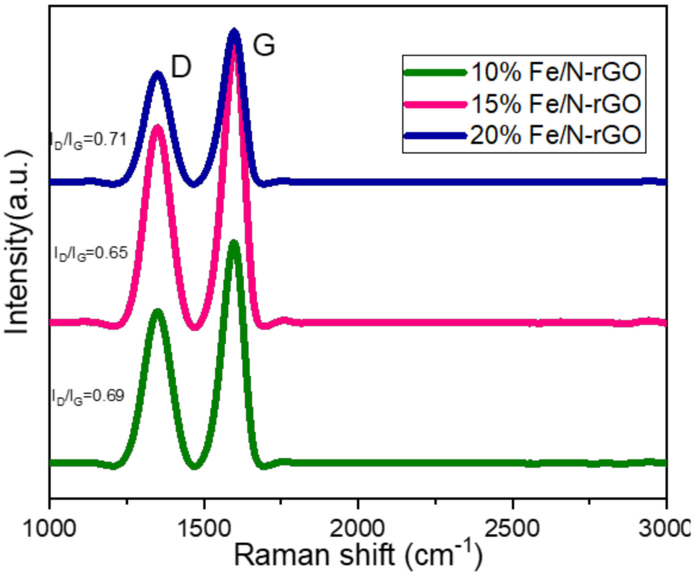

Figure 2. Raman spectra of D and G bands of 10% Fe/N-rGO, 15% Fe/N-rGO and 20% Fe/N-rGO.

Table 1. Energy dispersive spectroscopy (EDS) results presenting the elemental composition of X Fe/N-rGO (X = 10%, 15% and 20%).

Name of Samples	wt.% of C	wt.% of O	wt.% of Fe
10% Fe/N-rGO	71.22	24.37	4.41
15% Fe/N-rGO	86.85	11.50	2.10
20% Fe/N-rGO	76.65	13.43	9.92

3.3. Fourier Transform Infrared Spectroscopy Analysis

Fourier transform infrared (FTIR) spectroscopy was applied to determine the possible functional groups in the compositions. The FTIR spectra of the irradiated samples are depicted in Figure 3. All the three samples were composed of C–H (884.34 cm^{-1}), C–O (1127.35 cm^{-1}), C–C/C–N (1314.46 cm^{-1}), C=C (2158 cm^{-1}) and O–H (3668.94 cm^{-1}). C–N stretching confirmed the existence of a N atom in the composition and formed a weak bond with a carbon atom. No sharp peak was observed in 15% Fe/N-rGO, indicating the weaker bond between the two atoms. Furthermore, 10% Fe/N-rGO and 20% Fe/N-rGO exhibited a slightly sharp peak. The C–N bond in 15% Fe/N-rGO almost disappeared. Previous studies revealed the C–O stretching peak between 1028 and 1308 cm^{-1}, the C–H stretching peak between 500 and 1000 cm^{-1} and the O–H stretching peak after 3420 cm^{-1}. The peaks of C–O and O–H respectively found at ~1127.35 cm^{-1} and 3668.94 cm^{-1} could be ascribed to the deformation of rGO [38,39].

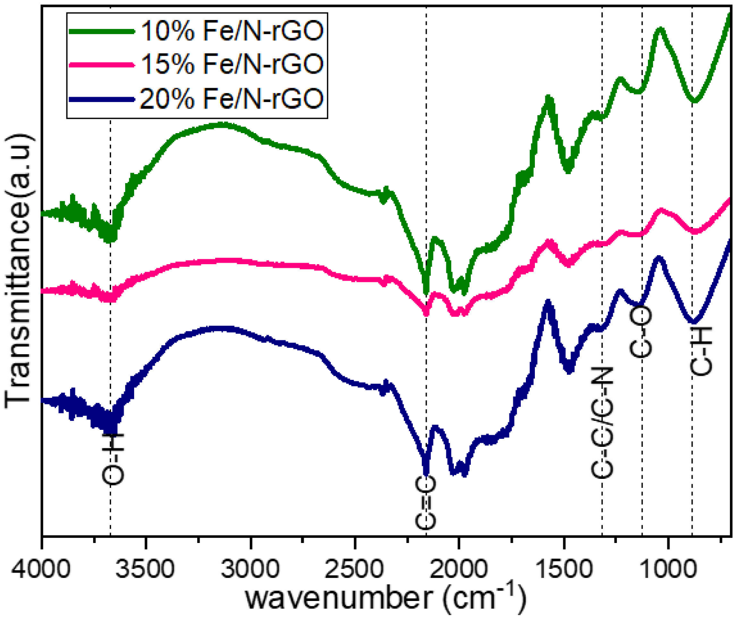

Figure 3. Fourier transform infrared (FTIR) spectra of 10% Fe/N-rGO, 15% Fe/N-rGO and 20% Fe/N-rGO.

3.4. Field Emission Scanning Electron Microscopy Analysis

Field emission scanning electron microscopy (FESEM)-EDS was conducted to examine the surface morphology and distribution of elements. The FESEM images of all the three samples are presented in Figure 4a–c. The surface of all the three samples was rough, folded and wrinkled, indicating that GO was reduced to rGO. This observation agreed with the XRD pattern shown in Figure 1a [18,26]. A few nanoscale iron particles were detected on the rGO surface in the micrographs. The lack of iron particles was probably due to the confinement of nanoparticles in the rGO interlayer or the lack of nitrogen-anchoring sites on rGO. The element mapping of 20% Fe/N-rGO via EDS is shown in the circulated area in Figure 4c and the distributions of Fe, C and O are illustrated in Figure 4d. The respective semiquantitative element distributions of all the samples are summarized in Table 1 to estimate the Fe loading on rGO. Approximately 50% of the designed Fe in all the samples except in 15% Fe/N-rGO was embedded onto rGO upon irradiation.

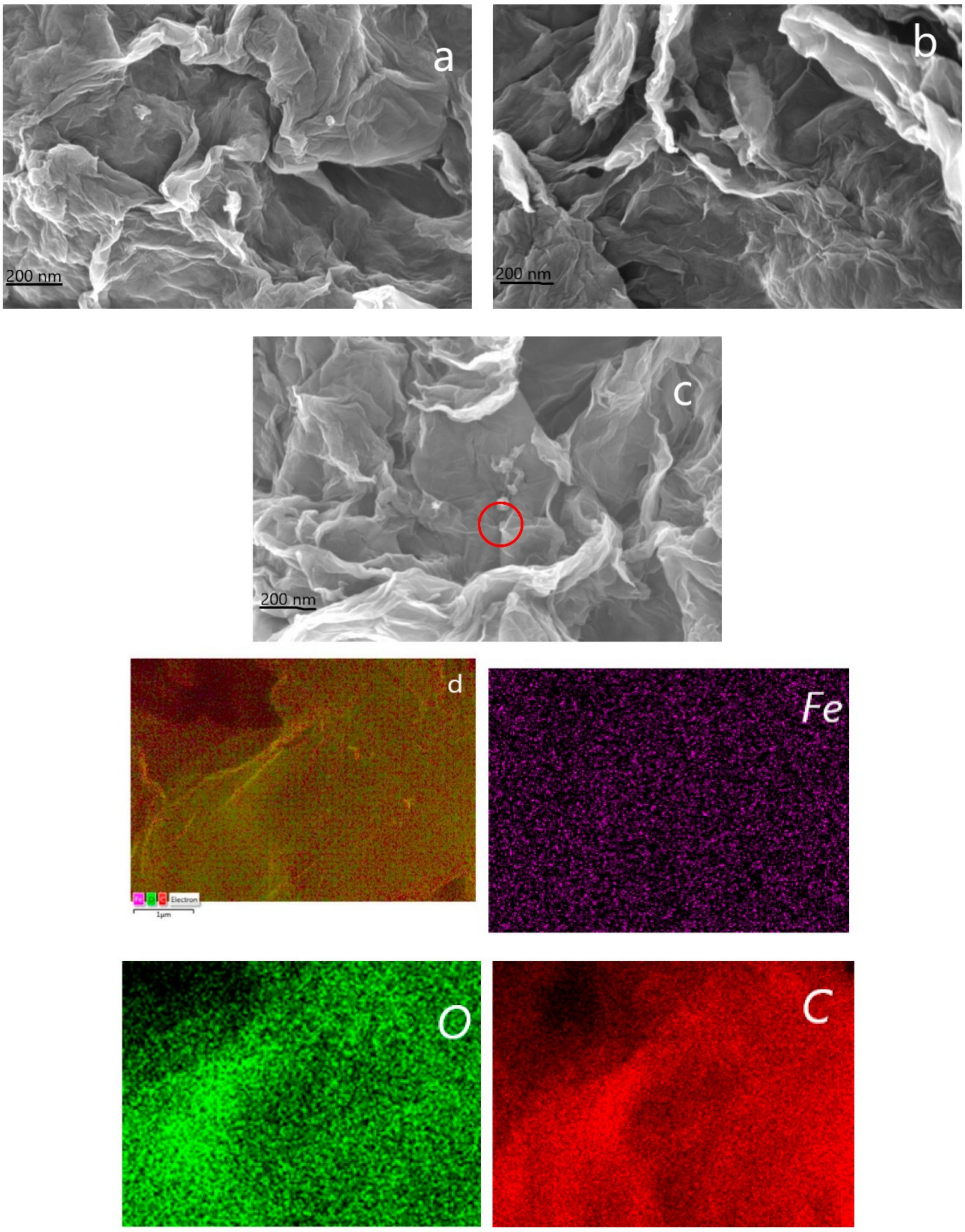

Figure 4. Surface morphology of (**a**) 10% Fe/N-rGO, (**b**) 15% Fe/N-rGO and (**c**) 20% Fe/N-rGO. (**d**) Element mapping of 20% Fe/N-rGO with its corresponding Fe, O and C.

3.5. Electrocatalytic Activity

The LSV curves of 10% Fe/N-rGO, 15% Fe/N-rGO and 20% Fe/N-rGO are presented in Figure 5a,c,e, respectively and their corresponding K–L plots at different potentials are illustrated in Figure 5b,d,f.

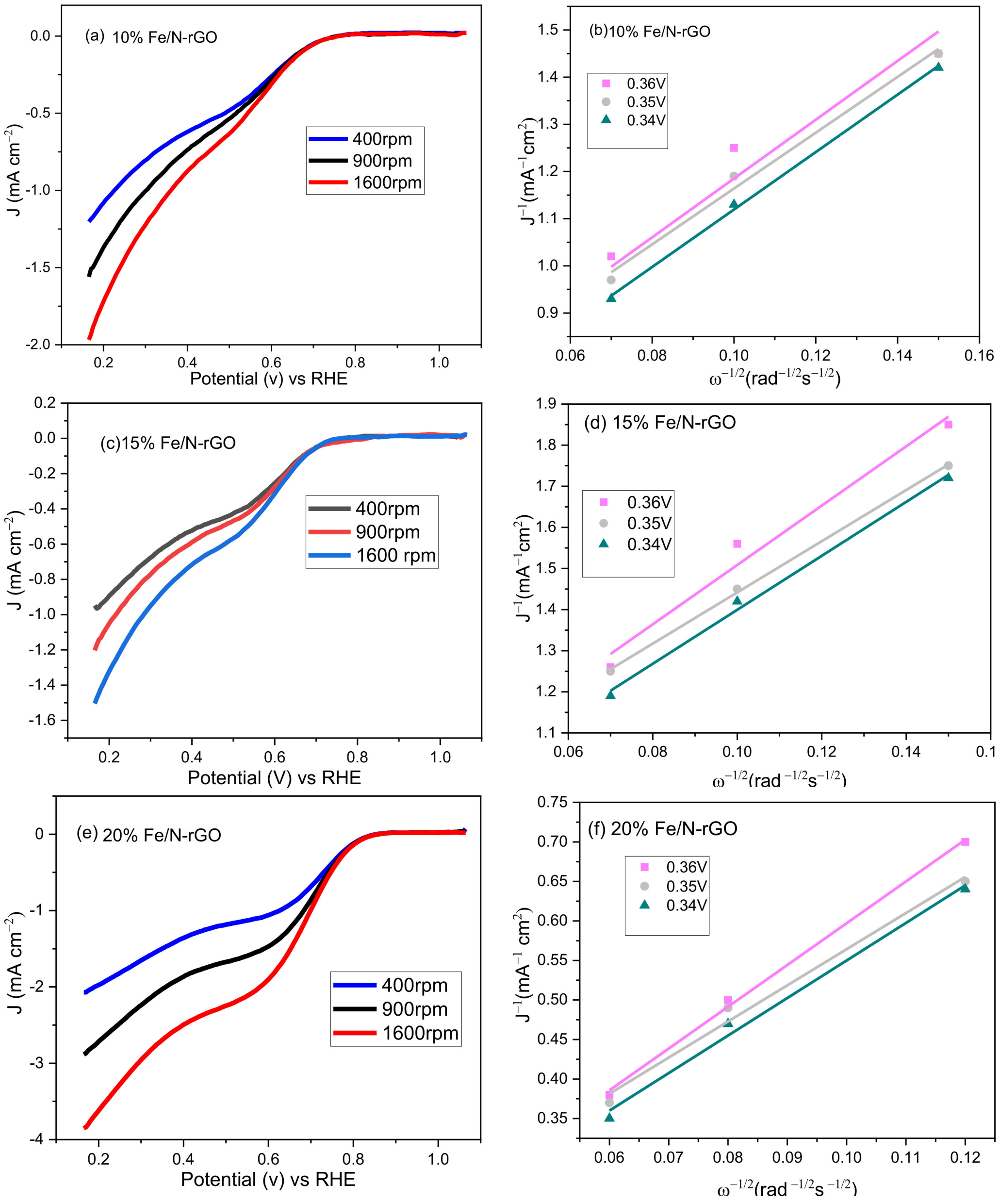

Figure 5. (**a**,**c**,**e**): Rotating disk electrode (RDE) measurement of the oxygen reduction reaction (ORR) of Fe/N-rGO catalyst with Fe loadings of 10%, 15% and 20% in O_2-saturated 0.1 M KOH, respectively. (**b**,**d**,**f**) Corresponding Koutecky–Levich plots at 0.34, 0.35 and 0.36 V (vs. RHE), respectively.

At 1600 rpm, 20% Fe/N-rGO exhibited the highest onset potential of 0.84 V (vs. RHE), whereas 15% Fe/N-rGO showed the lowest onset potentials 0.72 V (vs. RHE). The onset potential of 10% Fe/N-rGO was 0.74 V (vs. RHE). The onset potential of 20% Fe/N-rGO was comparable with those reported by Sudarsono et al. [7], Xi et al. [24] and Osmeiri et al. [25]. A higher onset potential indicated a higher catalytic activity. No limiting current plateau is observed in Figure 5a,c,e, indicating that the ORR in all the three samples was dominated by the mixed kinetics-diffusion controlled mechanism. Fe nanoparticles are possibly confined in rGO layers, so the active sites of nanoparticles may be hindered from participating in ORR. The ORR of these samples is also affected by the degree of carbon layer graphitization [40,41].

The number of electron transfers was estimated with the K–L plot at 0.34, 0.35 and 0.36 V (vs. RHE). A decent straight relationship could be observed between J^{-1} and $\omega^{-1/2}$ at various cathode potentials. The number of electron transfers was calculated using Equation (2) at the different electrode potentials. The results showed that 10%, 15% and 20% Fe/N-rGO had average electron transfers of 1.37, 1.26 and 2.25, respectively, suggesting that the preferred reaction pathway for these catalysts was two-electron reduction. This pathway could result in an reduction of oxygen to form peroxide ions (HO_2^-) as the final product. Jung et al. [42] have suggested that O_2 prefers to adsorb on single atom catalyst in "end-on" binding mode that hinders O-O bond breakage, which may be the case in our catalyst, judging from the EDS result. The rate of generating OH^- increases as the concentration of HO_2^- increases. The increasing trend of HO_2^- concentration leads to an increase in the dissolved Fe ion concentration [42,43]. These results contradicted some of the findings that suggested the four-electron reaction pathway for this type of catalyst. Similar to other non-pyrolyzed Fe-based catalysts, these catalysts have a very low catalytic activity for fuel cell applications [44]. This observation could be attributed to the lack of an appropriate ratio of doped N and the contribution of $Fe\text{-}N_x$. rGO needs a high amount of N because of its large surface area. N should be added to more than 60 wt.% of rGO [45]. The weight percent of urea was one-third of rGO; as such, no strong C–N sites were detected in this work. Adding metallic N could improve electron densities and develop N-supported sites with carbon and Fe, directly participating in ORR. The intense interaction between $Fe\text{-}N_x$ and O_2 facilitates a fast electron transfer. Fe_3C, N and Fe are important species to improve ORR [5,24,46–48].

4. Conclusions

In this work, we used a gamma irradiation method to synthesize N-doped rGO-supported Fe catalysts with different Fe loadings. Physicochemical characterizations via XRD, Raman spectroscopy, FTIR and EDS revealed that gamma irradiation could introduce N and Fe into the samples, although their optimum loadings were not achieved. K–L plot analysis suggested that the ORR of all the samples followed a two-electron transfer reaction pathway. The catalytic ORR was not as high as that in our previous works [7] possibly because of insufficient and underdeveloped active sites. In future studies, the concentration of N precursors should be increased so that higher amounts of N could be doped onto rGO, thereby increasing the anchor sites of Fe. This work also demonstrated that ORR was affected by Fe loading; that is, the higher the amount of Fe successfully loaded on rGO, the higher the ORR activity. However, further studies should be performed to optimize synthesis parameters.

Author Contributions: Conceptualization, K.L.L. and W.Y.W.; methodology, K.R.R.; validation, K.Y.K.; formal analysis, K.R.R.; investigation, K.R.R.; resources, K.L.L., K.Y.K., H.Y.; writing—original draft preparation, K.R.R.; writing—review and editing, K.L.L.; supervision, K.L.L.; project administration, K.L.L.; funding acquisition, K.L.L., K.Y.K., H.Y. All authors have read and agreed to the published version of the manuscript.

Funding: This research was funded by Universiti Kebangsaan Malaysia (GUP-2018-041 and PP-SELFUEL-2020), International Atomic Energy Agency (R23130), the Ministry of Science and Technology of Taiwan (MOST-108-3116-F-005-002) and SATU Joint Research Scheme (NCHU6).

Institutional Review Board Statement: Not applicable.

Informed Consent Statement: Not applicable.

Data Availability Statement: The data presented in this study are available on request from the corresponding author.

Conflicts of Interest: The authors declare no conflict of interest.

References

1. Hu, T.H.; Yin, Z.S.; Guo, J.W.; Wang, C. Synthesis of Fe nanoparticles on polyaniline covered carbon nanotubes for the oxygen reduction reaction. *J. Power Sources* **2014**, *272*, 661–671. [CrossRef]
2. Wen, Z.; Ci, S.; Zhang, F.; Feng, X.; Cui, S.; Mao, S.; Luo, S.; He, Z.; Chen, J. Nitrogen-enriched core-shell structured Fe/Fe 3C-C nanorods as advanced electrocatalysts for the oxygen reduction reaction. *Adv. Mater.* **2012**, *24*, 1399–1404. [CrossRef]

3. Villers, D.; Jacques-Bédard, X.; Dodelet, J.-P. Fe-based catalysts for Oxygen reduction in PEM fuel cells. *J. Electrochem. Soc.* **2004**, *151*, A1507–A1515. [CrossRef]
4. Park, M.; Lee, J.; Hembram, K.; Lee, K.-R.; Han, S.; Yoon, C.; Nam, S.-W.; Kim, J. Oxygen Reduction Electrocatalysts Based on Coupled Iron Nitride Nanoparticles with Nitrogen-Doped Carbon. *Catalysts* **2016**, *6*, 86. [CrossRef]
5. Gu, L.; Jiang, L.; Li, X.; Jin, J.; Wang, J.; Sun, G. A Fe-N-C catalyst with highly dispersed iron in carbon for oxygen reduction reaction and its application in direct methanol fuel cells. *Cuihua Xuebao Chin. J. Catal.* **2016**, *37*, 539–548. [CrossRef]
6. Dombrovskis, J.K.; Palmqvist, A.E.C. Recent Progress in Synthesis, Characterization, and Evaluation of Non-Precious Metal Catalysts for the Oxygen Reduction Reaction. *Fuel Cells* **2016**, *16*, 4–22. [CrossRef]
7. Sudarsono, W.; Wong, W.Y.; Loh, K.S.; Majlan, E.H.; Syarif, N.; Kok, K.Y.; Yunus, R.M.; Lim, K.L. Noble-free oxygen reduction reaction catalyst supported on Sengon wood (*Paraserianthes falcataria* L.) derived reduced graphene oxide for fuel cell application. *Int. J. Energy Res.* **2020**, *44*, 1761–1774. [CrossRef]
8. Fu, X.; Hassan, F.M.; Zamani, P.; Jiang, G.; Higgins, D.C.; Choi, J.Y.; Wang, X.; Xu, P.; Liu, Y.; Chen, Z. Engineered architecture of nitrogenous graphene encapsulating porous carbon with nano-channel reactors enhancing the PEM fuel cell performance. *Nano Energy.* **2017**, *42*, 249–256. [CrossRef]
9. Soo, L.T.; Loh, K.S.; Mohamad, A.B.; Daud, W.R.W.; Wong, W.Y. An overview of the electrochemical performance of modified graphene used as an electrocatalyst and as a catalyst support in fuel cells. *Appl. Catal. A Gen.* **2015**, *497*, 198–210. [CrossRef]
10. Molina-García, M.A.; Rees, N.V. Effect of catalyst carbon supports on the oxygen reduction reaction in alkaline media: A comparative study. *RSC Adv.* **2016**, *6*, 94669–94681. [CrossRef]
11. Shaari, N.; Kamarudin, S.K. Graphene in electrocatalyst and proton-conducting membrane in fuel cell applications: An overview. *Renew. Sustain. Energy Rev.* **2017**, *69*, 862–870. [CrossRef]
12. Alam, S.N.; Sharma, N.; Kumar, L. Synthesis of Graphene Oxide (GO) by Modified Hummers Method and Its Thermal Reduction to Obtain Reduced Graphene Oxide (rGO)*. *Graphene* **2017**, *6*, 1–18. [CrossRef]
13. Grigoriev, S.A.; Fateev, V.N.; Pushkarev, A.S.; Pushkareva, I.V.; Ivanova, N.A.; Kalinichenko, V.N.; Presnyakov, M.Y.; Wei, X. Reduced graphene oxide and its modifications as catalyst supports and catalyst layer modifiers for PEMFC. *Materials* **2018**, *11*, 1405. [CrossRef] [PubMed]
14. Vinayan, B.P.; Nagar, R.; Ramaprabhu, S. Synthesis, and investigation of the mechanism of platinum-graphene electrocatalysts by novel co-reduction techniques for proton exchange membrane fuel cell applications. *J. Mater. Chem.* **2012**, *22*, 25325–25334. [CrossRef]
15. Kumar, A.; Saini, A.; Sood, S.C.; Anand, V.K. Synthesis of Graphene Oxide using Modified Hummer's Method and its Reduction using Hydrazine Hydrate. *Int. J. Eng. Trends Technol.* **2016**, *40*, 67–71. [CrossRef]
16. Ban, F.Y.; Majid, S.R.; Huang, N.M.; Lim, H.N. Graphene oxide and its electrochemical performance. *Int. J. Electrochem. Sci.* **2012**, *7*, 4345–4351.
17. Park, H.Y.; Yang, D.S.; Bhattacharjya, D.; Song, M.Y.; Yu, J.S. A highly efficient carbon-supported Pt electrocatalyst prepared by γ-irradiation for cathodic oxygen reduction. *Int. J. Hydrogen Energy* **2014**, *39*, 1688–1697. [CrossRef]
18. Zhang, Y.; Ma, H.L.; Cao, K.; Wang, L.; Zeng, X.; Zhang, X.; He, L.; Liu, P.; Wang, Z.; Zhai, M. Gamma irradiation-induced preparation of Graphene-Ni nanocomposites with efficient electromagnetic wave absorption. *Materials* **2018**, *11*, 2145. [CrossRef]
19. He, Y.; Li, J.; Li, L.; Li, J. Gamma-ray irradiation-induced reduction and self-assembly of graphene oxide into three-dimensional graphene aerogel. *Mater. Lett.* **2016**, *177*, 76–79. [CrossRef]
20. Abidin, Z.; Muhamad, E.; Ahmad Daud, N.; Ibrahim, N.; Chieng, B.; Talib, Z. Functionalizing Graphene Oxide with Alkylamine by Gamma-ray Irradiation Method. *Nanomaterials* **2017**, *7*, 135. [CrossRef]
21. Wang, W.; Zhao, X.; Shi, H.; Liu, L.; Deng, H.; Xu, Z.; Tian, F.; Miao, X. Shape inducer-free polygonal angle platinum nanoparticles in graphene oxide as oxygen reduction catalyst derived from gamma irradiation. *J. Colloid Interface Sci.* **2020**, *575*, 1–15. [CrossRef] [PubMed]
22. Minitha, C.R.; Rajendrakumar, R.T. Synthesis, and Characterization of Reduced Graphene Oxide. *Adv. Mater. Res.* **2013**, *678*, 56–60. [CrossRef]
23. Soo, L.T.; Loh, K.S.; Mohammad, A.B.; Doud, W.R.W.; Wong, W.Y. Effect of nitrogen precursors on the electrochemical performance of nitrogen-doped reduced graphene oxide towards oxygen reduction reaction. *J. Alloys Compd.* **2016**, *677*, 112–120. [CrossRef]
24. Xi, J.; Wang, F.; Mei, R.; Gong, Z.; Fan, X.; Yang, H.; An, L.; Wu, Q.; Luo, Z. Catalytic performance of a pyrolyzed graphene supported Fe–N–C composite and its application for acid direct methanol fuel cells. *RSC Adv.* **2016**, *6*, 90797–90805. [CrossRef]
25. Osmieri, L.; Videla, A.M.; Specchia, S. The use of different types of reduced graphene oxide in the preparation of Fe-N-C electrocatalysts: Capacitive behavior and oxygen reduction reaction activity in alkaline medium. *J. Solid State Electrochem.* **2016**, *20*, 3507–3523. [CrossRef]
26. Peng, H.; Mo, Z.; Liao, S.; Liang, H.; Yang, L.; Luo, F.; Song, H.; Zhong, Y.; Zhang, B. High-performance Fe- and N- Doped carbon catalyst with graphene structure for oxygen reduction. *Sci. Rep.* **2013**, *3*, 1–7. [CrossRef]
27. Ren, G.; Gao, L.; Teng, C.; Li, Y.; Yang, H.; Shui, J.; Lu, X.; Zhu, Y.; Dai, L. Ancient Chemistry "pharaoh's Snakes" for Efficient Fe-/N-Doped Carbon Electrocatalysts. *ACS Appl. Mater. Interfaces* **2018**, *10*, 10778–10785. [CrossRef]
28. Saleem, H.; Haneef, M.; Abbasi, H.Y. Synthesis route of reduced graphene oxide via thermal reduction of chemically exfoliated graphene oxide. *Mater. Chem. Phys.* **2018**, *204*, 1–7. [CrossRef]

29. Kar, T.; Devivaraprasad, R.; Singh, R.K.; Bera, B.; Neat, M. Reduction of graphene oxide-a comprehensive electrochemical investigation in alkaline and acidic electrolytes. *RSC Adv.* **2014**, *4*, 57781–57790. [CrossRef]
30. Ma, C.; Yang, K.; Wang., L.; Wang, X. Facile synthesis of reduced graphene oxide/ Fe_3O_4 nanocomposite film. *J. Appl. Blomater. Funct. Mater.* **2017**, *15*, S1–S6. [CrossRef]
31. Chung, Y.Y.; Loh, K.S.; Daud, W.R.W.; Mohamad, A.B. Synthesis and Characterization of Sulfonated Graphene Oxide Nanofiller for Polymer Electrolyte Membrane. *IOP Conf. Ser. Mater. Sci. Eng.* **2016**, *160*. [CrossRef]
32. Tong, J.; Li, Y.; Bo, L.; Wang, W.; Li, T.; Zhang, Q. Core-shell Fe_3O_4@NCS-Mn derived from chitosan-Schiff based mn complex with enhanced catalytic activity for the oxygen reduction reaction. *Catalysts* **2019**, *9*, 692. [CrossRef]
33. Wang, Q.; Ma, Y.; Liu, L.; Yao, S.; Wu, W.; Wang, Z.; Lv, P.; Zheng, J.; Yu, K.; Wei, W.; et al. Plasma enabled Fe2O3/Fe3o4 nano-aggregates anchored on nitrogen-doped graphene as anode for sodium-ion batteries. *Nanomaterials* **2020**, *10*, 782. [CrossRef] [PubMed]
34. Aujara, K.M.; Chieng, B.W.; Ibrahim, N.A.; Zainuddin, N.; Ratnam, C.T. Gamma-irradiation induced functionalization of graphene oxide with organosilanes. *Int. J. Mol. Sci.* **2019**, *20*, 1910. [CrossRef] [PubMed]
35. Tang, F.; Lei, H.; Wang, S.; Wang, H.; Jin, Z. A novel Fe-N-C catalyst for efficient oxygen reduction reaction based on polydopamine nanotubes. *Nanoscale* **2017**, *9*, 17364–17370. [CrossRef]
36. Ngidi, N.P.D.; Ollengo, M.A.; Nyamori, V.O. Effect of Doping Temperatures and Nitrogen Precursors on the Physicochemical, Optical, and Electrical Conductivity Properties of Nitrogen-Doped Reduced Graphene Oxide. *Materials* **2019**, *12*, 3376. [CrossRef]
37. Boas, C.R.S.V.; Focassio, B.; Marinho, E.; Larrude, D.G.; Salvadori, M.C.; Leao, C.R.; Santos, D.J. Characterization of nitrogen-doped graphene bilayers synthesized by fast, low-temperature microwave plasma-enhanced chemical vapor deposition. *Sci. Rep.* **2019**, *9*, 1–12.
38. Rochman, R.A.; Wahyuningsih, S.; Ramelan, A.H.; Hanif, Q.A. Preparation of nitrogen and sulfur Co-doped reduced graphene oxide (rGO-NS) using N and S heteroatom of thiourea. *IOP Conf. Ser. Mater. Sci. Eng.* **2019**, *509*. [CrossRef]
39. Sun, M.; Davenport, D.; Liu, H.; Qu, J.; Elimelech, M.; Li, J. Highly efficient and sustainable non-precious metal Fe-N-C electrocatalyst for oxygen reduction reaction. *J. Mater. Chem. A* **2018**, *6*, 2527–2539. [CrossRef]
40. Xiao, M.; Zhu, J.; Feng, L.; Liu, C.; Xing, W. Meso/macroporous nitrogen-doped carbon architectures with iron carbide encapsulated in graphitic layers as an efficient and robust catalyst for the oxygen reduction reaction in both acidic and alkaline solutions. *Adv. Mater.* **2015**, *27*, 2521–2527. [CrossRef] [PubMed]
41. He, H.; Zhong, Y.; Liang, X.; Tan, W.; Zhu, J.; Wang, C.Y. Natural Magnetite: An efficient catalyst for the degradation of organic contaminant. *Sci. Rep.* **2015**, *5*, 10139. [CrossRef] [PubMed]
42. Jung, E.; Shin, H.; Antink, W.H.; Sung, Y.E.; Hyeon, T. Recent Advances in Electrochemical Oxygen Reduction to H_2O_2: Catalyst and Cell Design. *ACS Energy Lett.* **2020**, *6*, 1881–1892. [CrossRef]
43. Qaseem, A.; Chen, F.; Wu, X.; Johnston, R.L. Pt-free Silver Nonalloy Electrocatalyst for Oxygen Reduction Reaction in Alkaline Media. *Catal. Sci. Technol.* **2016**, *6*, 3317–3340. [CrossRef]
44. Qiao, Y.; Ni, Y.; Kong, F.; Li, R.; Zhang, C.; Kong, A.; Shan, Y. Pyrolytic Carbon-coated Cu-Fe Alloy Nanoparticles with High Catalytic Performance for Oxygen Electroreduction. *Chem. Asian J.* **2019**, *14*, 2676–2684. [CrossRef]
45. Chen, Z.; Higgins, D.; Yu, A.; Zhang, L.; Zhang, J. A review of non-precious metal electrocatalysts for PEM fuel cells. *Energy Environ. Sci.* **2011**, *4*, 3167–3192. [CrossRef]
46. Basri, S.; Kamarudin, S.K. Nanocatalyst FeN4/C Molecular Orbital Behaviour for Oxygen Reduction Reaction (ORR) in Cathode Direct Methano Fuel Cell (DMFC). *J. Kejuruter. SI.* **2018**, *1*, 59–64. [CrossRef]
47. Chong, S.T.; Lee, T.K.; Samad, S.; Loh, K.S.; Wong, W.Y.; Wan Daud, W.R.; Sunarso, J. Carbon and non-carbon support materials for platinum-based catalysts in fuel cells. *Int. J. Hydrogen Energy* **2018**, *43*, 7823–7854. [CrossRef]
48. Guo, D.; Han, S.; Wang, J.; Zhu, Y. MIL-100-Fe derived N-doped Fe/Fe 3 C@C electrocatalysts for the efficient oxygen reduction reaction. *Appl. Surf. Sci.* **2018**, *434*, 1266–1273. [CrossRef]